Band structure theory of the bcc to hcp Burgers distortion

Bojun Feng and Michael Widom

Band Structure Theory of the BCC to HCP Burgers Distortion

Bojun Feng and Michael Widom

Department of Physics, Carnegie Mellon University, Pittsburgh, PA 15213

Abstract

The Burgers distortion is a two-stage transition between body centered cubic (BCC) and hexagonal close-packed (HCP) structures. Refractory metal elements from the Sc and Ti columns of the periodic table (BCC/HCP elements) form BCC structures at high temperatures but transition to HCP at low temperatures via the Burgers distortion. Elements of the V and Cr columns, in contrast, remain BCC at all temperatures. The energy landscape of BCC/HCP elements exhibits an alternating slide instability, while the normal BCC elements remain stable as BCC structures. This instability is verified by the presence of unstable elastic constants and vibrational modes for BCC/HCP elements, while those elastic constants and modes are stable in BCC elements. We show that a pseudogap opening in the density of states at the Fermi level drives the Burgers distortion in BCC/HCP elements, suggesting the transition is of the Jahn-Teller-Peierls type. The pseudogap lies below the Fermi level for regular BCC elements in the V and Cr columns of the periodic table. The wave vector $\mathbf{k}_S$ when the gap opens relates to the reciprocal lattice vector $\mathbf{G}=(1\ \frac{1}{2}\ \frac{1}{2})$ of the distorted BCC structure as $\mathbf{k}_S=\frac{1}{2}\mathbf{G}$. BCC binary alloys containing both BCC/HCP and BCC elements exhibit a similar instability but stabilize part way through the BCC to HCP transition.

I. INTRODUCTION

Elements from the Sc and Ti columns of periodic table are body centered cubic (BCC) at high temperatures and transform to hexagonal close-packed (HCP) at low temperatures. We refer to these as BCC/HCP elements. Their transition is known as the Burgers distortion [1]. On the other hand, elements from the V and Cr columns are BCC at all temperature below their melting temperatures. Although prior works discuss the BCC to HCP transition, (e.g. angular distortive matrices [2], space group representation [3], pressure-induced transitions [4–8], MD simulation [9]) and a review of instability of metal elements [10] including Burgers and Bain instabilities, a complete understanding including the electronic structure driving the transition is missing. We seek the underlying cause of the instability in order to understand the mechanical properties of refractory metals and their alloys, especially high entropy alloys (HEAs) containing both BCC/HCP and normal BCC elements [11]. Our study is also complementary to the previous work of Lee and Hoffmann [12] who discussed a Jahn-Teller type transition of transition metals and alloys from BCC to FCC structures. While they focus on transition metals starting from V column going to the right of the periodic table, corresponding to the BCC to FCC transition, our study goes to the left of the periodic table. However, both transitions share similar pseudo-gap opening and bonding/antibonding orbital stabilization.

The Burgers distortion is a two-stage transition, consisting of an orthorhombic shear deformation and an alternating slide displacement between atomic layers of the BCC structure [13]. We sketch the mechanism in Fig. 1. In the notation of Ref. [13], a Pearson type oS4 cell characterized by two variables, λ_1 and λ_2, interpolates between the BCC and HCP structures. The lattice constants of this oS4 cell are

$$a(\lambda_1) = a_0/\alpha(\lambda_1), \quad b(\lambda_1) = \alpha(\lambda_1)\sqrt{2}a_0, \quad c = \sqrt{2}a_0 \tag{1}$$

where a, b and c are the three lattice constants of the oS4 cell, $\alpha(\lambda_1) = 1 + (\sqrt[4]{3/2} - 1)\lambda_1$, and a_0 is the lattice constant of the corresponding BCC structure. Notice that the lattice constants of the oS4 cell only depend on the value of λ_1 and their variation generates orthorhombic shear. The positions of the four atoms in the oS4 cell are

$$\mathbf{R}_1 = (0, \frac{3+\lambda_2}{12}b, \frac{1}{4}c) \qquad\qquad \mathbf{R}_2 = (0, -\frac{3+\lambda_2}{12}b, -\frac{1}{4}c)$$

$$\mathbf{R}_3 = (\frac{1}{2}a, \frac{\lambda_2-3}{12}b, \frac{1}{4}c) \qquad\qquad \mathbf{R}_4 = (\frac{1}{2}a, \frac{3-\lambda_2}{12}b, -\frac{1}{4}c). \tag{2}$$

λ_2 generates the alternating slide between atomic layers in (1,1,0) planes of BCC. When $\lambda_1 = \lambda_2 = 0$, we have a BCC structure (Pearson type cI2), and the oS4 cell is a $1 \times \sqrt{2} \times \sqrt{2}$ supercell of BCC. When $\lambda_1 = \lambda_2 = 1$, the structure is HCP (Pearson type hP2).

Both λ_1 and λ_2 alter bond bond lengths. Nearest neighbor (NN) and next nearest neighbor (NNN) bonds are of particular importance. To understand the instability of the BCC structure, we consider their variation for small distortions. Expanding to first order in λ_1 and λ_2 we find

$$NN_L \equiv |\mathbf{R}_1 - \mathbf{R}_3| \approx \frac{\sqrt{3}}{2}a_0 + \frac{1}{12}(6^{3/4} - 2\sqrt{3})a_0\lambda_1 \tag{3}$$

$$NN_S \equiv |\mathbf{R}_1 - \mathbf{R}_4| \approx \frac{\sqrt{3}}{2}a_0 - \frac{1}{12}(6^{3/4} - 2\sqrt{3})a_0\lambda_1$$

$$NNN_L \equiv |\mathbf{R}_1 - \mathbf{R}_2| \approx a_0 + \frac{1}{6}a_0\lambda_2$$

$$NNN_S \equiv |\mathbf{R}_3 - \mathbf{R}_4| \approx a_0 - \frac{1}{6}a_0\lambda_2$$

Notice that both the NN and NNN bonds split into long and short versions (subscripts L and S, respectively, in Eq. 3), with the NN bonds varying to first order only in λ_1, and the NNN bonds varying to first order only in λ_2.

In the following sections, we examine the impact of electronic structure on the total energy as λ_1 and λ_2 vary during the Burgers distortion. We show that λ_2 distortion drives the initial instability of the BCC structure, by opening a gap in the electronic band structure, creating a pseudo-gap in the electronic density of state and a charge density wave, with subsequent relaxation in the λ_1 variable that eventually stabilizes an HCP structure. We recognize the initial instability as a type of Jahn-Teller-Peierls distortion [14–17]. We then turn to alloys and show how the BCC structure of binary alloys containing both BCC/HCP and normal BCC elements are stabilized part way through Burgers the distortion.
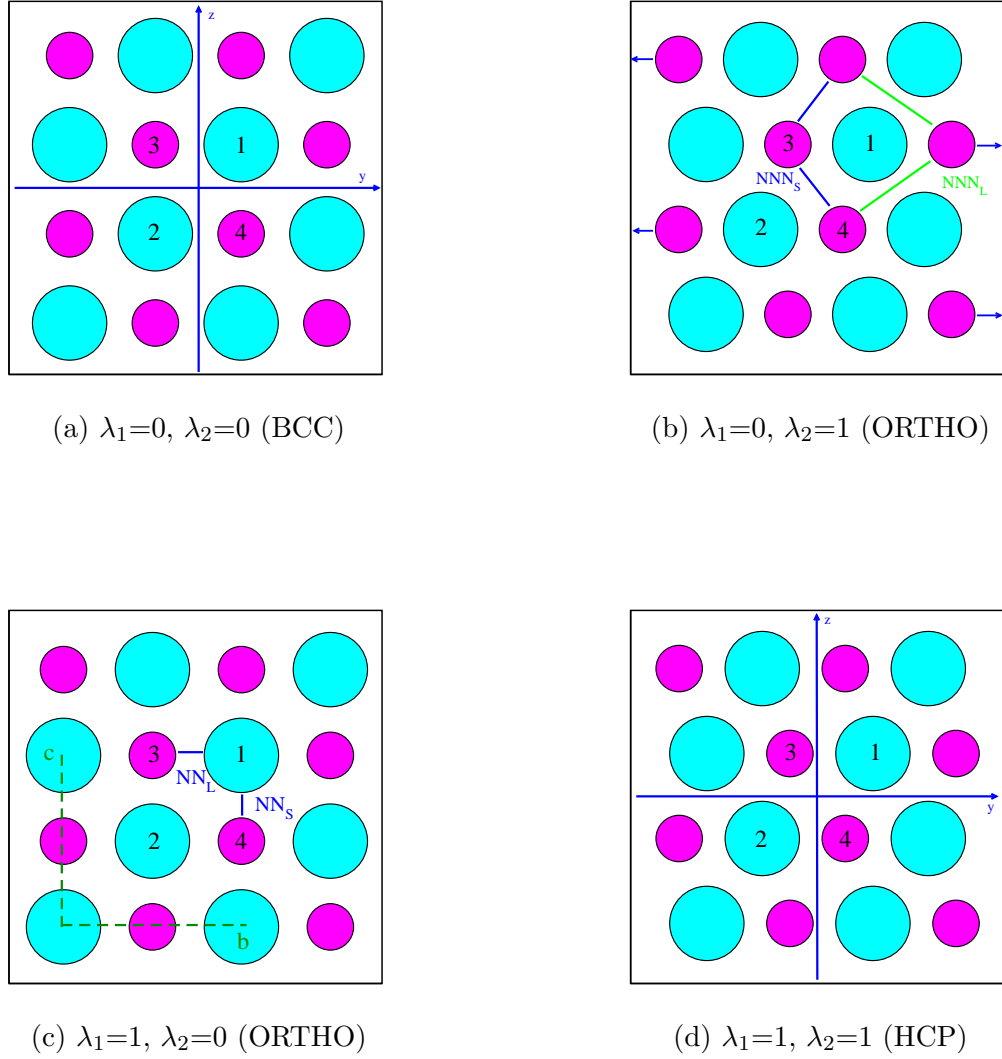
(a) $\lambda_1=0$, $\lambda_2=0$ (BCC)

(b) $\lambda_1=0$, $\lambda_2=1$ (ORTHO)

(c) $\lambda_1=1$, $\lambda_2=0$ (ORTHO)

(d) $\lambda_1=1$, $\lambda_2=1$ (HCP)

FIG. 1: Illustration of the Burgers distortion. (a) $\sqrt{2} \times \sqrt{2} \times 1$ supercell of BCC viewed along the [1,0,0] direction; (b) Alternating slide displacement; (c) Orthorhombic shear b>c; (d) unit cell of HCP structure viewed along the [1,0,0] direction. Large cyan atoms are in lower layer; small magenta atoms are in upper layer. For pure element all atoms are same species; for binary alloys, magenta and cyan are BCC/HCP and normal BCC, respectively. Atoms are labeled according to Eq. 2.

II. PURE ELEMENTS

A. Elasticity and Phonons

1. Elasticity

We begin our analysis with calculation of BCC/HCP and normal BCC refractory element T=0K elastic constants. These are obtained within density functional theory from stress-strain relationships using two-point central differences as implemented in VASP [18]. We employ the generalized gradient approximation (GGA [19]) without spin polarization. The energy cutoffs of the plane wave basis sets are set to 400eV and k-point meshes are set to 14×14×14 in 16-atom 2×2×2 supercells of the conventional 2-atom unit cell. We use "Accurate" precision to avoid wraparound errors. An extensive set of elastic constants for these metals and many more crystalline compounds is available in reference [20] and in the references of reference [10].

As shown in Table I, BCC/HCP elements from the Sc and Ti columns have $C_{11} \leq C_{12}$. This violates a Born stability condition and predicts instability to a tetragonal or orthorhombic distortion. These elements are stabilized in the BCC state at high temperature by their vibrational entropy [21]. The BCC structures become mechanically unstable at low temperatures, causing the transformation to HCP. Elements from the V and Cr columns all have $C_{11} > C_{12}$, so that the BCC structures are maintained at low temperatures. Note that our calculations underestimate C_{44} for V and Nb, which arises from the combined effects of Fermi surface nesting, an electronic topological transition and the Jahn-Teller effect [22–24].

2. Phonon Instability

We calculate the Γ-point phonon modes of the 2×2×2 supercell structures using density functional perturbation theory (DFPT) [25]. Fig. 2 illustrates the unstable modes of Hf and Table II lists the unstable phonon mode frequencies for all HCP/BCC elements. Each of the BCC/HCP elements has a 6-fold degenerate imaginary frequency mode, and three of them also have a second 6-fold degenerate lower imaginary frequency mode. All BCC elements are stable as BCC structures with no imaginary frequency modes. In every case the (maximal) imaginary frequency mode corresponds to the λ_2 alternating slide deformation illustrated

5

moduli	C_{11}	C_{12}	C_{44}	C_{11}	C_{12}	C_{44}	C_{11}	C_{12}	C_{44}	C_{11}	C_{12}	C_{44}
element	Sc			Ti			V			Cr		
moduli	59	59	27	99	119	41	317	163	28	580	175	119
element	Y			Zr			Nb			Mo		
moduli	25	46	22	92	96	34	250	139	17	517	181	117
element	La			Hf			Ta			W		
moduli	-14	47	7	77	118	54	270	163	77	525	205	147

element	frequency	element	frequency
Sc	$2.73i$	Ti	$3.21i$, $4.93i$
Y	$2.05i$	Zr	$2.50i$
La	$1.76i$, $1.80i$	Hf	$1.80i$, $2.76i$

in Fig. 1b. We can understand the 6-fold degeneracy because we have three choices for the direction of alternation (*i.e.* $\hat{x}, \hat{y}$, or $\hat{z}$ in Fig. 1) and for each direction of alternation we have two choices of perpendicular direction in which to displace. Equivalently, the cubic crystal system has 6 independent but symmetry equivalent {111} planes within which to slide. This mode reduces the symmetry from cubic to orthorhombic. If the initial cubic structure is displaced according to this mode, it follows the Burgers distortion pathway and relaxes to HCP. The lower imaginary frequency mode corresponds to a tetragonal symmetry breaking. If the initial cubic structure is displaced according to this mode it follows the Bain path to either a tI2 or an FCC structure. Complete phonon dispersion relations of several refractory metals are presented in reference [26].
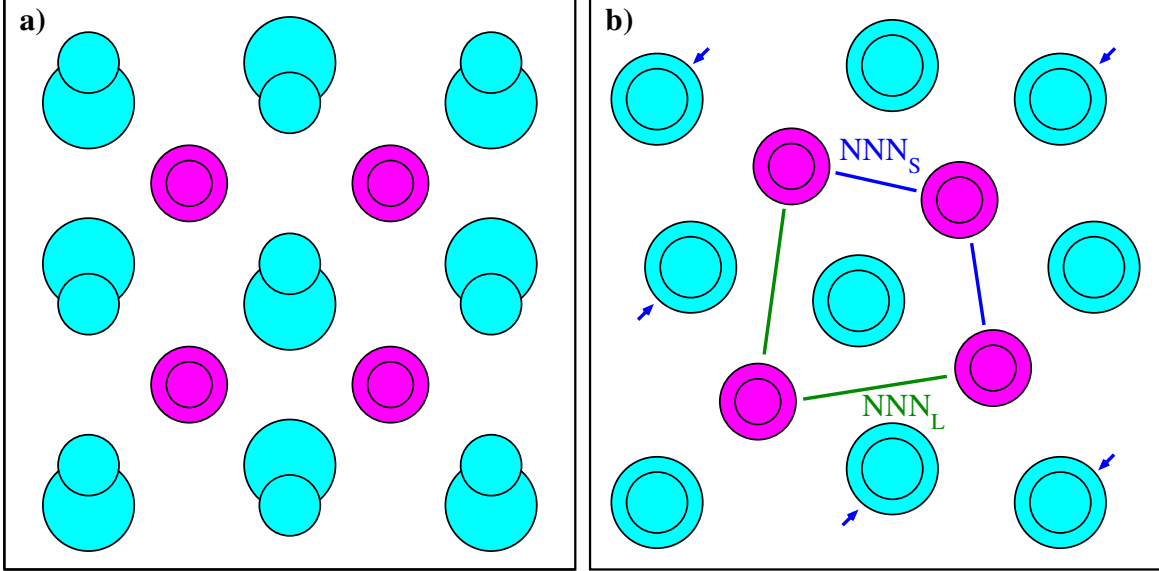
FIG. 2: Unstable phonon modes of Hf in $2 \times 2 \times 2$ supercell of conventional BCC unit cell viewed along the cubic [100] axis. Note the y and z axes are rotated by 45° compared with Fig. 1. Atom sizes indicate vertical height. Colors distinguish cube vertex (magenta) from cube center (cyan). (a) Lower imaginary frequency. (b) Upper imaginary frequency.

3. Energy Landscape

The instabilities of the BCC/HCP elements can be seen from their energy landscapes as the λ_1 and λ_2 values are varied (see Fig. 3). These are calculated within the conventional oS4 unit cell using $12 \times 8 \times 8$ k-point meshes and otherwise normal VASP defaults. Specifically, only lattice volume is relaxed, but not cell shape or ion position, in order to maintain the λ_1 and λ_2 values. BCC/HCP elements are more stable as HCP structures, while BCC elements are more stable as BCC structures. Notice that the Burgers distortion is driven initially by the λ_2 distortion, since if we start from BCC ($\lambda_1 = 0$, $\lambda_2 = 0$), changing λ_2 reduces the energy much more quickly than changing λ_1 does. Thus the Burgers distortion should begin in the λ_2 direction (alternating slide), then later complete in the λ_1 direction (variation of lattice parameters).

Fig. 3 presents energy landscapes for the Ti and V columns of the periodic table. Similar behaviors are found in the Sc and Cr columns, although in the case of the Sc column the initial instabilities in λ_1 are somewhat stronger than those in the Ti column.
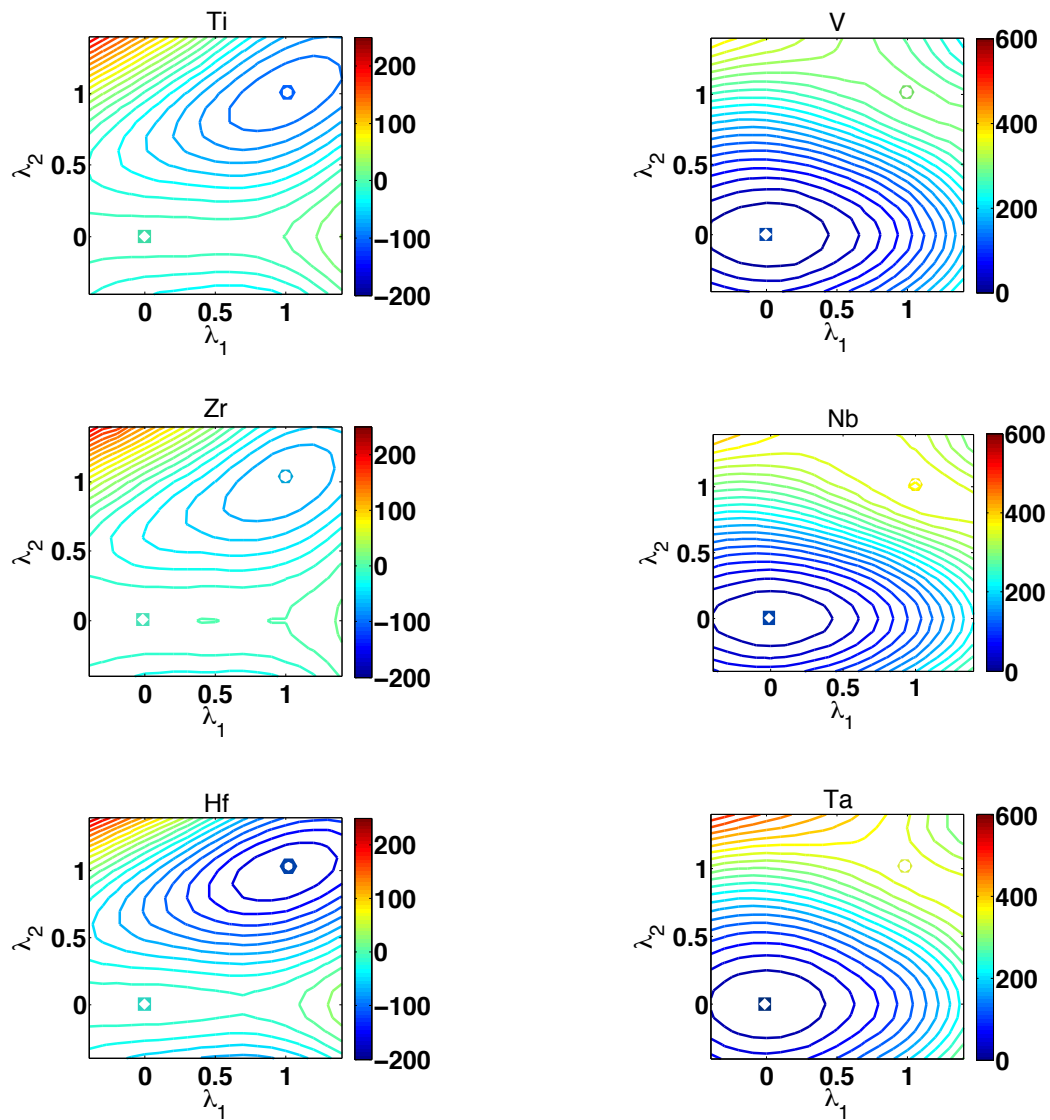
FIG. 3: Energy landscapes of elements from the Ti (left) and V (right) columns of the periodic table. Elements from the Ti column are stable as HCP (hexagons), whereas elements from the V column are stable as BCC (squares). Color bars give energy contours in meV/atom relative to energies of the BCC structures.
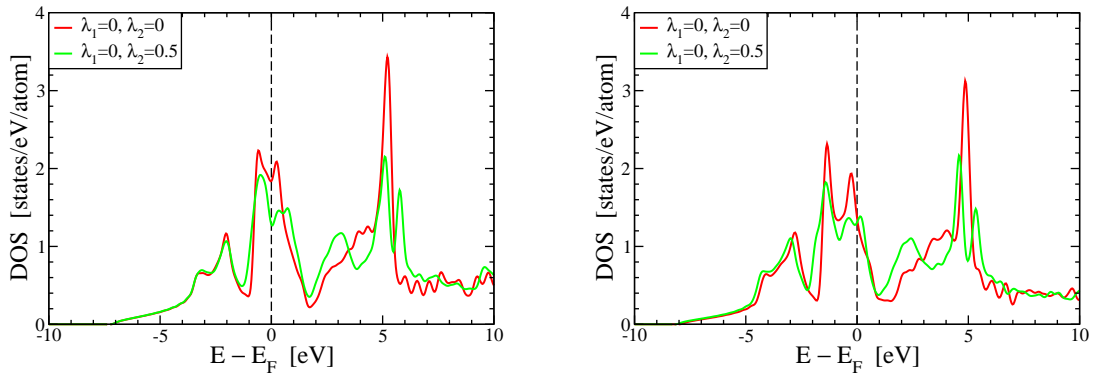
FIG. 4: DOS comparison of Hf (left) and Ta (right) before and after the application of λ_2 distortion.

B. Electronic Structure

So far, our investigation of elasticity, phonon modes and energy landscapes has illustrated the instability of BCC/HCP elements without revealing the underlying mechanism. Here, we seek an explanation by examining the electronic structure. Our study focuses on the HCP/BCC element Hf and the normal BCC element Ta. Our findings for Ta apply equally to the entire V and Cr columns of the periodic table, while our findings for Hf apply to the entire Ti column, and with minor modification (discussed later), to the Sc column.

1. Density of States

The electronic density of states (DOS) is qualitatively similar for Hf and Ta, although the Fermi energy, E_F, is higher for Ta owing to its extra valence electron. Hf has a weak pseudogap right at E_F, while this pseudogap lies below E_F in the case of Ta. The pseudogap deepens upon application of the λ_2 distortion, as illustrated in Fig. 4. Thus, in the case of Hf, increasing λ_2 reduces the energy of occupied states below E_F while raising the energy of empty states above E_F, and hence lowering the band energy [27–29] relative to the initial BCC structure [30–32]. The band energy of Ta is less strongly affected, because the pseudogap opening occurs below E_F.

The impact of λ_2 on total energy $E_{Total}(\lambda_2)$ is quantified in Table III for Hf and Ta. Here E_0 refers to values at $\lambda_2 = 0$. Owing to the symmetry between $\pm\lambda_2$, all first derivatives with

TABLE III: Energy contributions E_0 to BCC Hf and Ta, and their second variation as λ_2 varies from -0.1 to 0.1. αZ and E_{Ewald} give the electrostatic energy of the ions in the electron gas. V_H is the Hartree potential. $E_{xc} - V_{xc}$ and PAW_{dc} are double counting corrections. E_{band} is the sum of Kohn-Sham eigenvalues, and E_{atom} is an arbitrary offset approximating the energy of an isolated atom. Units are eV/atom.

	Hf		Ta	
Contribution	E_0	$\Delta^2 E / \Delta \lambda_2^2$	E_0	$\Delta^2 E / \Delta \lambda_2^2$
αZ	86.33	-9.46	125.99	-13.20
E_{Ewald}	-742.93	+29.64	-956.72	+36.59
$-V_H$	-104.39	-8.50	-112.11	-13.37
$E_{xc} - V_{xc}$	20.13	-0.47	22.79	-0.47
PAW_{dc}	11.14	-0.42	13.63	-0.06
E_{band}	-140.89	-11.79	-152.54	-8.67
E_{atom}	860.87	0	1047.14	0
E_{Total}	-9.72	-0.98	-11.80	+0.78

respect to λ_2 vanish. Hence, we approximate their second derivatives by taking a second central difference using $\lambda_2 = \pm 0.1$ and 0. The total energy is the sum of several large terms with opposing signs. Most contributions are decreasing functions of λ_2, with the exception of the Ewald energy of repulsion among the positively charged ions which increases due to the short second neighbor bonds. The repulsion is stronger for Ta than for Hf. Among the negative contributions, the band energy stands out as being stronger for Hf than for Ta. Notice the relative signs of total energy variation, confirming the instability of Hf and the stability of Ta.

2. Band Structure

Pseudogap opening in the DOS results from a gap opening in the band structure. Fig. 5 plots the band structures of Hf and Ta at λ_2=0 and 0.1. These are calculated using the oS4 primitive cell. Fig. 6 displays the Brillouin zone of the BCC structure in the oS4 setting with $\lambda_2 = 0$, and table IV gives coordinates of the special points [33]. Because oS4 is a supercell
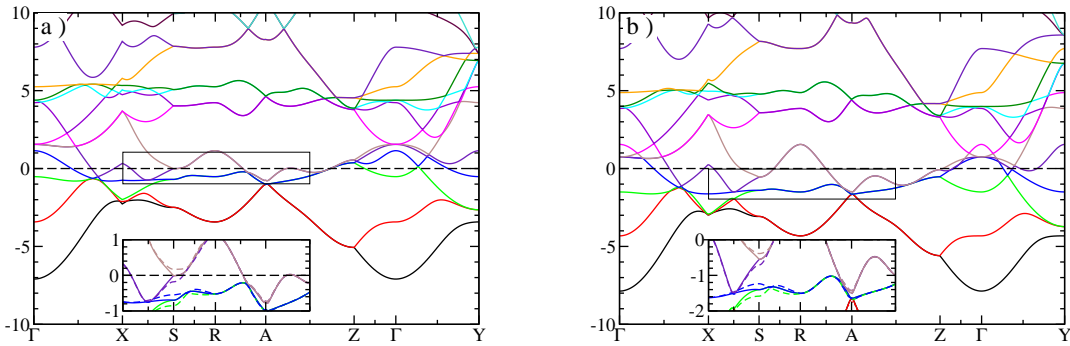
FIG. 5: Band structure comparison of (a) Hf and (b) Ta. See Fig. 6 and Table IV for special point locations. The insets enlarge the vicinity of the special point S. Solid bands show $\lambda_2 = 0$ (*i.e.* BCC in an oS4 setting) while dashed bands (see inset) show $\lambda_2 = 0.1$.

of BCC, the usual BCC Brillouin zone is folded. The BCC special points map onto special points of oS4, so that the BCC 4x point H appears at the oS4 point Y; the BCC 2x point N appears at the oS4 points Γ, R and Y; the BCC 3x point P appears at a position 2/3 of the way along the oS4 special line ΓX.

As λ_2 increases, a band-gap opens up between degenerate states at the S point, reflecting the DOS pseudo-gap opening both in Hf and in Ta. For Hf, the gap opens at E_F so that occupied states drop in energy while empty states rise. In contrast, the extra electron in Ta places E_F above the gap so that the drop in energy is partially offset by the increase in energy of some occupied states. Hence λ_2 has a greater influence on band energy for Hf than for Ta.

Since λ_2 reduces the symmetry from cubic to orthorhombic, we recognize the the energy reduction by gap opening as a bulk crystalline analogue of the Jahn-Teller distortion. According to Jahn and Teller [14], breaking the symmetry of a molecule can split a partially occupied highest molecular orbital (HOMO), resulting in a drop in energy of the HOMO and increase in energy of the split-off lowest unoccupied molecular orbital (LUMO). Equivalently, from the point of view of Peierls [15], symmetry breaking creates a gap in a partially filled band, reducing the energy of occupied states and increasing the energy of unoccupied states. Hence we recognize the mechanical instability of BCC Hf as a manifestation of the Jahn-Teller-Peierls mechanism.
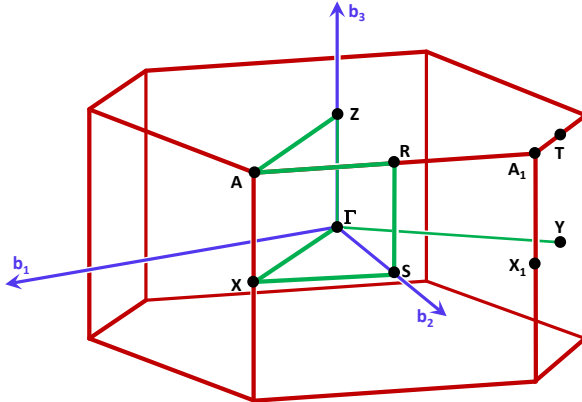
11

FIG. 6: Brillouin zone of oS4 with $b = c = \sqrt{2}a$. See Table IV for coordinates of special points.

TABLE IV: Symmetry k-points of the oS4 cell [33]. $\zeta = (1 + a^2/b^2)/4 = \frac{3}{8}$ for the case $a = b$.

$\times\mathbf{b_1}$	$\times\mathbf{b_2}$	$\times\mathbf{b_3}$		$\times\mathbf{b_1}$	$\times\mathbf{b_2}$	$\times\mathbf{b_3}$	
0	0	0	Γ	-1/2	1/2	1/2	T
ζ	ζ	1/2	A	ζ	ζ	0	X
$-\zeta$	$1-\zeta$	1/2	A_1	$-\zeta$	$1-\zeta$	0	X_1
0	1/2	1/2	R	-1/2	1/2	0	Y
0	1/2	0	S	0	0	1/2	Z

We examined all the elements in the Sc-Cr columns of the periodic table. The entire Ti column shows the same two band degeneracies at the S-point that is lifted by λ_2 as seen in Hf. These degenerate points fall below E_F throughout the entire V and Cr columns which contain, respectively, one and two electrons more than the Ti column. For the Ti column, the upper degenerate point sits just at E_F. In the case of the trivalent elements of the Sc column, which contain one electron less than the Ti column, E_F lies just slightly above the lower degenerate point. In view of their mechanical instability we suspect that proximity to the degenerate point is sufficient to drive the BCC to HCP distortion. Thus we expect
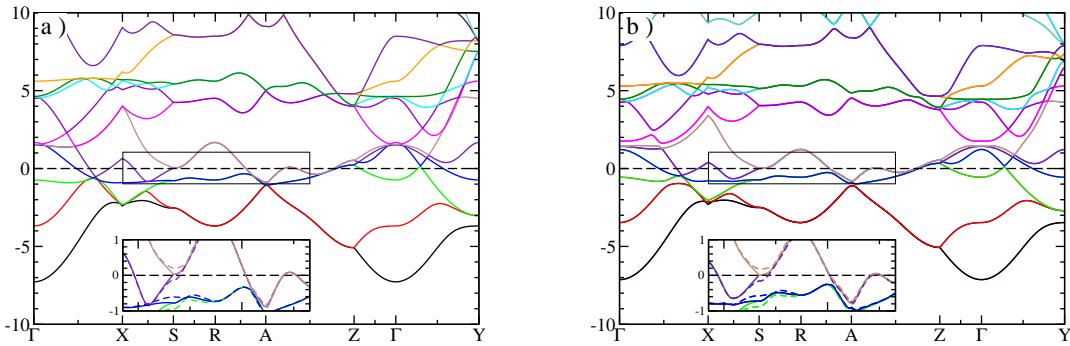
FIG. 7: Band structure comparison of Hf using (a) LDA and (b) Spin-orbit coupling. See Fig. 6 and Table IV for special point locations. The insets enlarge the vicinity of the special point S. Solid bands show $\lambda_2 = 0$ (*i.e.* BCC in an oS4 setting) while dashed bands (see inset) show $\lambda_2 = 0.1$.

similar behavior across the rare earth series, all of which can be trivalent and all of which exhibit transitions from BCC at high temperature to either HCP or FCC.

Because the precise band energies can be influenced by the choice of exchange correlation functional, we pesent the band structure of Hf in the local density approximation (LDA [34]) in Fig. 7a. Similarly, because spin-orbit coupling is strong for $5d$ metals and can split degenerate bands, we present the band structure of Hf in the generalized gradient approximation (GGA [19]) with spin-orbit coupling in Fig. 7b. In both cases, the degenerate state with $\lambda_2 = 0$ is maintained at the special point S at E_F, and the band-gap opens up for $\lambda_2 > 0$.

3. Wave Function and Charge Density

With $\lambda_2 = 0$, the oS4 structure shown in Fig. 1a becomes BCC, as can be verified from its diffraction pattern illustrated in Fig. 8. As λ_2 grows, superlattice peaks appear and grow in amplitude proportionally to λ_2. In real space the structure evolves an alternating pattern of short and long next nearest neighbor bonds (see Fig. 1b). Notice that this alternation doubles the periodicity along the y-axis of the charge density integrated over x and z. The peak at the lowest k value arises at position $\mathbf{G} = \mathbf{b}_2 = 2\mathbf{k}_S$ in the notation of oS4 (see Table IV) where $\mathbf{k}_S$ is the position of the S point. This oS4 reciprocal lattice vector is
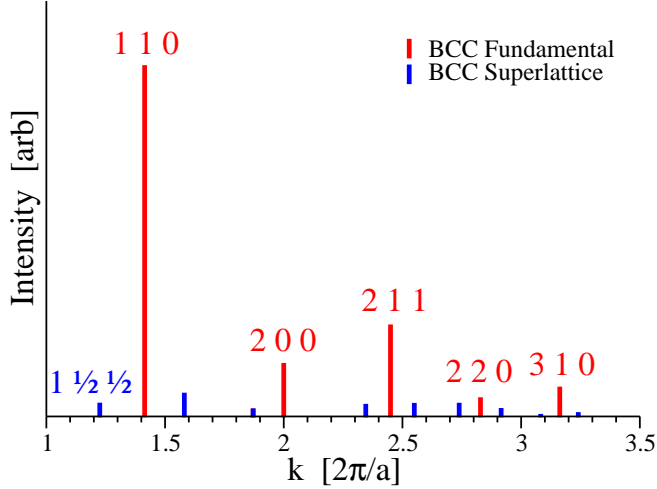
13

FIG. 8: Diffraction pattern of oS4 with $\lambda_2 = 0.5$. With $\lambda_2 = 0$ only BCC peaks (red) are present, while superlattice peaks (blue) grow linearly in λ_2. Peaks are indexed according to their positions within the conventional cubic unit cell.

equivalent to the super lattice peak ($hkl = 1\frac{1}{2}\frac{1}{2}$) in conventional cubic unit cell indexing.

The modulation of the potential at wavevector $\mathbf{b}_2$ couples the degenerate electron states $\psi_{\mathbf{k}}(\mathbf{r}) = e^{i\mathbf{k}\cdot\mathbf{r}}u_{\mathbf{k}}(\mathbf{r})$ of wave vectors $\mathbf{k} = \mathbf{k}_S$ and $-\mathbf{k}_S$ to first order in perturbation theory, leading to standing wave states that can localize in regions of low potential in the vicinity of the short NNN bonds, and thereby reducing their energy to first order in λ_2. Short NNN bonds are strengthened (*i.e.* are more electron dense) and long NNN bonds are weakened. Figure 9 plots the wavefunctions of the occupied and empty states that split off from E_F at the S-point (*i.e.* the dashed brown and indigo lines in Fig. 5a) in the yz-plane passing through an atomic layer. $\psi_{\mathbf{k}}$ turn out to be real functions at the special k-point. This plot reveals that they have d_{yz} character in the vicinity of the atoms.

For the occupied state (dashed purple in Fig. 5a), the sign of the wavefunction (Fig. 9a) alternates between atoms connected by short NNN_S bonds, so that the signs of the lobes of adjacent d_{xy} orbitals match, creating bonding states with high electron density (Fig. 9b) adjacent to the bonds between the atoms. In contrast, the sign of the wavefunction does not reverse along NNN_L bonds, causing the signs of the lobes of the d_{xy} orbitals to conflict, leading to low electron density between the atoms. The higher energy unoccupied state (dashed brown in Fig. 5a) exhibits the opposite behavior (Fig. 9c, d), with charge density
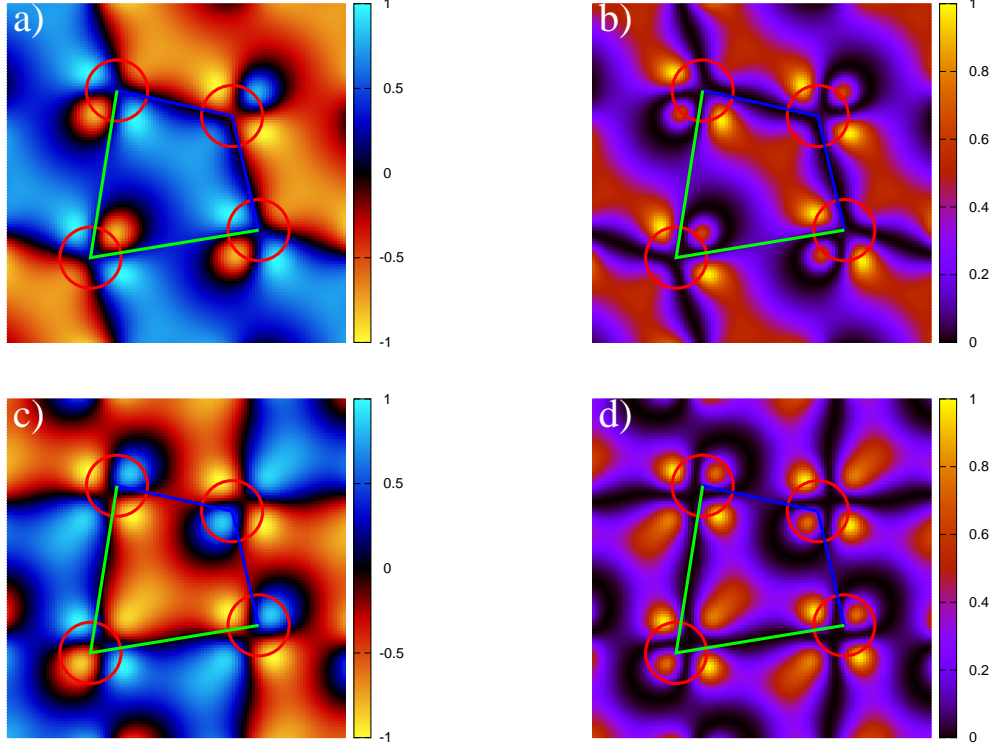
FIG. 9: S-point wavefunctions of Hf with $\lambda_2 = 0.5$. The figures show a 2×2 supercell of the conventional cubic unit cell in the same orientation as Fig. 2. a) and b) show the occupied state while c) and d) show the empty state. a) and c) show the real functions $\psi_{\mathbf{k}_S}(\mathbf{r})$; b) and d) show the electron density $|\psi_{\mathbf{k}_S}(\mathbf{r})|^2$. The wavefunctions were obtained from VASP using WaveTrans [35]. The red circles represent the position of atoms, and blue/green lines are bonding of the shortened/enlongated NNN bonds.

concentrating adjacent to the long NNN_L bonds. The entire effect is a three-dimensional version of the classical Peierls transition [36].

A similar effect is observed in Ta (not shown), because setting $\lambda_2 \neq 0$ necessarily creates a superlattice. However, in the case of Ta, both the upper and lower states of broken degeneracy remain occupied, so the impact on band structure energy is reduced.

TABLE V: Elastic constants (units of GPa) and unstable phonon frequencies (units of THz) of TiV, NbZr and HfTa alloys in the cP2 structure. The left frequencies correspond to the mode in Fig. 2a, while the right ones corresponds to Fig. 2b

Alloy	Frequencies	C_{11}	C_{12}	C_{44}
TiV	$3.44i$, $3.43i$	174	125	31
NbZr	$1.17i$, $2.41i$	153	110	19
HfTa	$2.04i$, $2.28i$	153	136	54

III.   BINARY ALLOYS

A.   Elasticity, Phonons and Energy Landscape

Given the instability of the BCC/HCP elements and the stability of the normal BCC elements, it is interesting to examine alloys containing both BCC/HCP and BCC elements. In this section, we discuss binary alloys taking the Pearson type cP2 structure with BCC/HCP elements at cube vertices and normal BCC elements at body centers.

Elasticity and phonon calculations for TiV, NbZr and HfTa binaries are summarized in Table V. The cubic elastic constants obey the Born stability rules; $C_{11}+2C_{12} > 0$, $C_{11} > C_{12}$ and $C_{44} > 0$. However, there are two unstable phonon modes in the 2x2x2 cell, equivalent to those illustrated for pure elements in Fig. 2. The modes with the upper imaginary frequencies have degeneracy 6, and correspond to the same alternating slide displacement as in the pure elemental case. The modes with the lower imaginary frequencies have degeneracy 3, rather than 6, because only the normal BCC elements displace. Presumably this is because the large HCP/BCC atoms force a large cubic lattice constant, and the smaller normal BCC atoms displace to shorten the next-nearest neighbor bond lengths.

Taking the same oS4 structure as in Eqs. 1 and 2, setting atoms $\mathbf{R}_1$ and $\mathbf{R}_2$ to BCC/HCP while $\mathbf{R}_3$ and $\mathbf{R}_4$ to normal BCC, $\lambda_1 = \lambda_2 = 0$ is a cP2 structure, while $\lambda_1 = \lambda_2 = 1$ corresponds to a Pearson type oP4 structure with atoms at HCP positions but with the symmetry reduced to orthorhombic due to the chemical order. Fig. 10 shows the energy landscapes of these binary alloys. Unlike the pure BCC/HCP elements and pure BCC elements, neither the BCC nor the HCP structures are stable. Instead, the BCC structures start with the
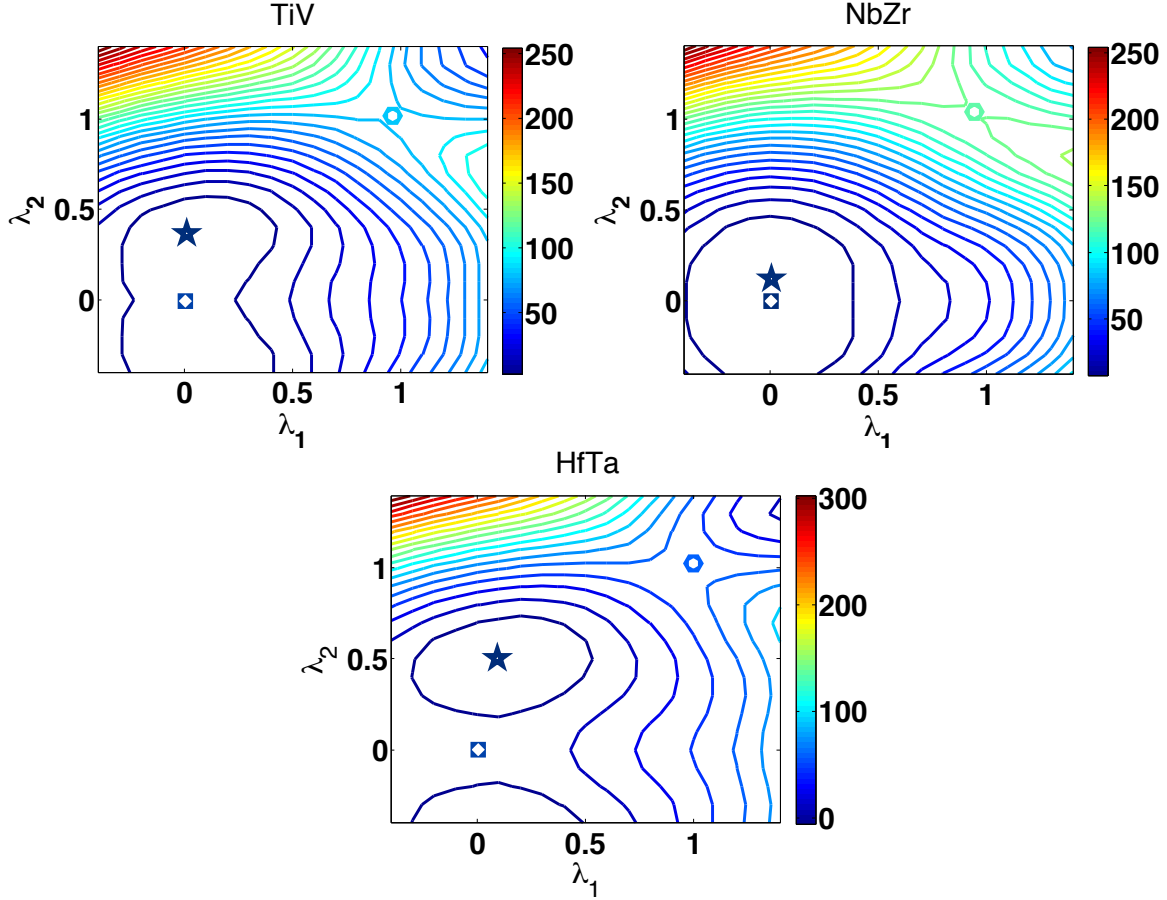
FIG. 10: Energy landscapes of TiV, NbZr and HfTa (square: cP2, hexagon: oP4, star: most stable state). The colorbars give the relative stability with respect to the BCC structures.

same λ_2 instability as in the pure BCC/HCP element case, but the transformation gets "stuck" part way through. The atoms displace part way along λ_2 while leaving λ_1 nearly 0, and these stable states are shown as stars in Fig. 10.

B.   Electronic Structure

As in Fig. 4 for pure elements, we show the DOS of HfTa before and after the λ_2 distortion (λ_2=0.5) in Fig. 11. Notice that the DOS has a similar shape to pure Hf and Ta, while the Fermi energy lies 0.5eV above the pseudo-gap, compared with 0eV in the case of Hf and 1eV in the case of Ta. As in the case of pure elements, λ_2 deepens the pseudogap and shifts occupied states to lower energies.
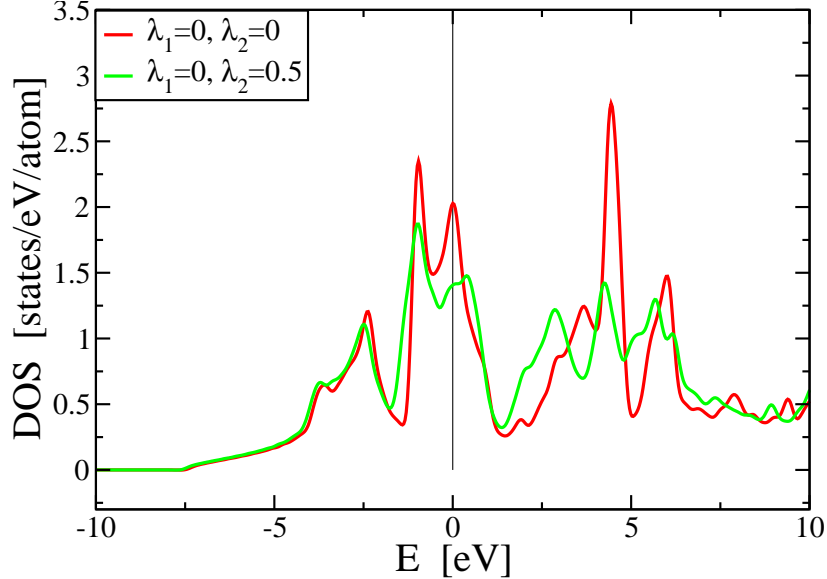
FIG. 11: DOS comparison of HfTa before and after the application of λ_2 distortion.

Fig. 12 shows the band structure of HfTa before and after the λ_2 distortion ($\lambda_2=0.1$). At the S point, brown and orange states correspond to the brown state in the pure Hf and Ta cases (Fig. 5), and indigo and magenta states correspond to the indigo state in Hf and Ta. It worth mentioning that, in the binary alloy cases, in order to achieve Pearson type cP2 structure, a 4-atom unit cell of pearson type oS4 cell is required. Since a 2-atom primitive cell of pearson type oS4 cell is used for pure element cases, the number of bands doubles for binary alloys compared with the pure elements. For binary alloys, before any λ_2 distortion at S point, these four states already split into two sets of two-fold degenerate states because of the symmetry breaking of the inequivalent atomic sites, but this band gap opening does not stabilize the binary because the gap opening happens below the Fermi energy. After λ_2 distortion, those two sets of two-fold degenerate states further split because of the further symmetry breaking that both nearest and next nearest neighbor distance become inequivalent like shown in Fig. 1. This band gap opening makes the purple state below the Fermi energy while the cyan state rises to slightly higher than the Fermi energy, and this accounts for the fact that λ_2 distortion lowers the net energy of binary HfTa.

Table VI breaks down the alloy total energy into individual contributions, as was done for pure elements in Table III. Again, the electrostatic energy (first three terms) of ionic repulsion stabilizes the BCC structure, while the band energy stands out as a strong desta-
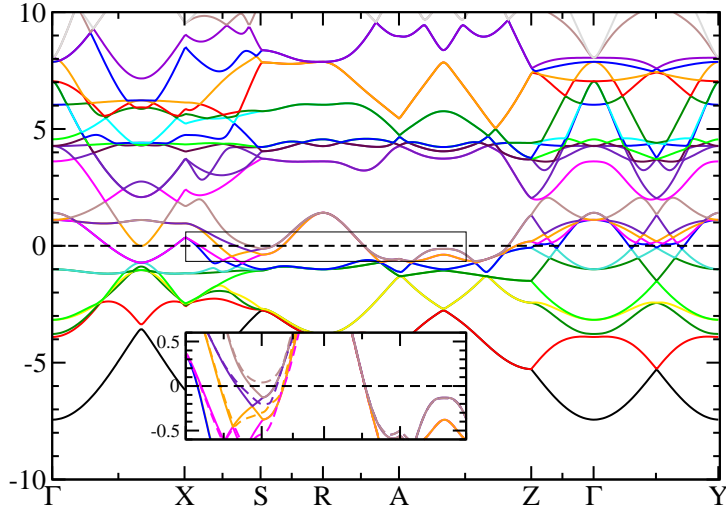
FIG. 12: Band structure comparison of HfTa before and after the application of λ_2 distortion.

bilizing factor. The net variation $\Delta^2 E/\Delta\lambda_2^2 < 0$ exhibits instability that is weaker than in the case of pure Hf.

Bonding effects in the wave functions at $\mathbf{k}_S$ are similar to those observed in Hf and Ta, as shown in Fig. 13.

IV. CONCLUSIONS

This paper describes a complete mechanism of the Burgers distortion of BCC/HCP elements that are stable at high temperatures due to the their vibrational entropy but transition to HCP at low temperatures. The two-stage distortion occurs through an alternating slide displacement between (110) atomic layers followed by relaxation of lattice parameters. The instability is apparent in the violation of elastic stability criteria and the presence of unstable imaginary frequency phonon modes in the BCC state. Electronic structure investigation explains how the distortion lowers the energy: a pseudo-gap in the electronic density of states, a band gap opening at a high symmetry k-point, and drop in energy of an occupied bonding state *vs.* increased energy of an empty antibonding state.

TABLE VI: Energy contributions E_0 to cP2 HfTa, and their second variation as λ_2 varies from -0.1 to 0.1. αZ and E_{Ewald} give the electrostatic energy of the ions in the electron gas. V_H is the Hartree potential. $E_{xc} - V_{xc}$ and PAW_{dc} are double counting corrections. E_{band} is the sum of Kohn-Sham eigenvalues, and E_{atom} is an arbitrary offset approximating the energy of an isolated atom. Units are eV/atom.

Contribution	E_0	$\Delta^2 E/\Delta\lambda_2^2$
αZ	105.02	-2.50
E_{Ewald}	-847.38	+9.74
$-V_H$	-109.77	-4.58
$E_{xc} - V_{xc}$	21.47	-0.07
PAW_{dc}	12.51	-0.38
E_{band}	-146.52	-2.66
E_{atom}	954.00	0
E_{Total}	-10.66	-0.36

These effects are similar to the Jahn-Teller instability of molecules that break symmetry to lower the energy of their highest occupied molecular orbital, and are also a three dimensional version of the Peierls instability that creates a superlattice structure in order to open a band gap that lowers the total band energy. They are most striking in tetravalent refractory metals from the Ti column of the periodic table, because in this case the degenerate point sits very close to the Fermi energy. They are also present in the trivalent refractory metals of the Sc column, because in these cases a second degenerate point sits about 0.1 eV below E_F. By similar reasoning the effect should be present across the trivalent Lanthanide rare earth series, and we have confirmed this in the case of Lu.

This work does not address the high temperature stability in the BCC state due to vibrational entropy. The imaginary modes prevent application of usual techniques for vibrational free energy calculation. Sophisticated techniques are required to incorporate the strong phonon anharmonicity [37, 38] in order to explain stability of BCC at high temperatures. Our present study addressed the instability in the limit of T=0K. While the electronic state degeneracy and splitting that we report remain present at the temperatures of the BCC to HCP transformation, conceivably some additional phonon-related effect could enter as
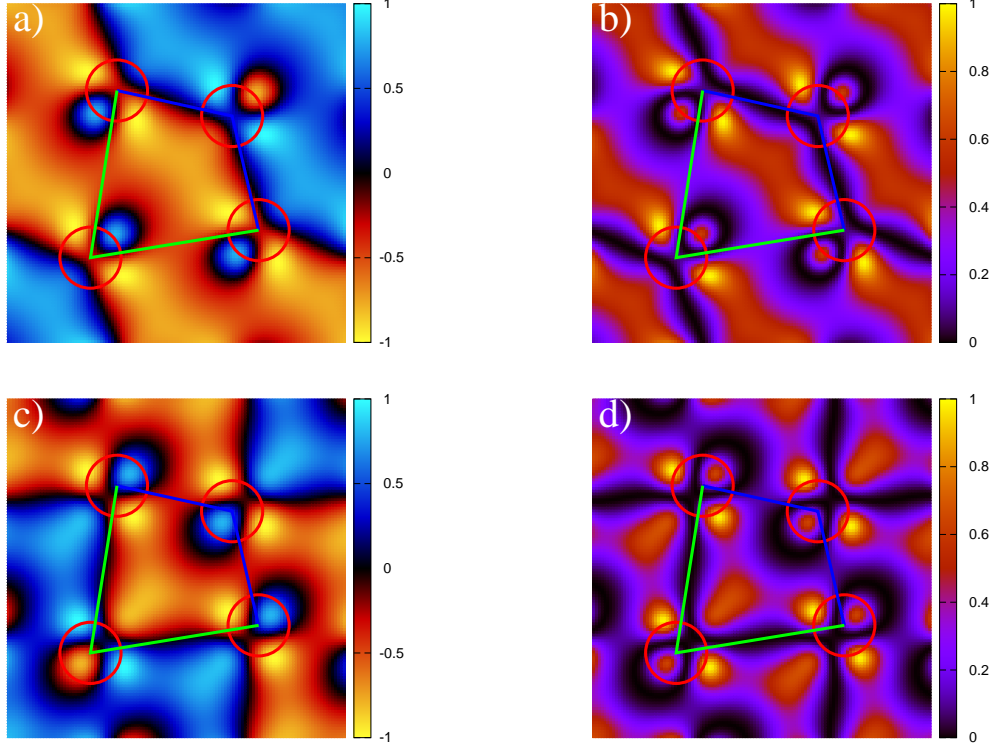
FIG. 13: S-point wavefunctions of HfTa with $\lambda_2 = 0.5$. The figures show a 2×2 supercell of the conventional cubic unit cell in the same orientation as Fig. 2. a) and b) show the occupied state (indigo in Fig. 12) while c) and d) show the empty state (brown in Fig. 12). a) and c) show the real function $\psi_{\mathbf{k}_S}(\mathbf{r})$; b) and d) show the electron density $|\psi_{\mathbf{k}_S}(\mathbf{r})|^2$. The wavefunction was obtained from VASP using WaveTrans [35]. The red circles represent the position of atoms, and blue/green lines are bonding of the shortened/enlongated NNN bonds.

well. Normal BCC elements from the V and Cr columns have extra valence electrons so that their Fermi energies sit well above the degenerate points. In these cases, ionic and electronic repulsion prevent the instability, and their BCC structures are stable at all temperatures.

Finally, we addressed the case of alloys containing both BCC/HCP and normal BCC elements. In this case the instability remains and leads to distortions in atomic positions while leaving lattice constants almost cubic. Perhaps this effect can explain the large lattice distortions reported [11] in refractory high entropy alloys containing BCC/HCP elements.

21

REFERENCES

[1] W. Burgers, On the process of transition of the cubic-body-centered modification into the hexagonal-close-packed modification of zirconium, Physica 1 (1934) 561–586.

[2] C. Cayron, Angular distortive matrices of phase transitions in the FCC–BCC–HCP system, Acta Mat. 111 (2016) 417–441.

[3] S. Srinivasan, D. Hatch, H. Stokes, A. Saxena, R. Albers, T. Lookman, Mechanism for BCC to HCP transformation: generalization of the burgers model, arXiv preprint cond-mat/0209530.

[4] D. F. Johnson, E. A. Carter, Nonadiabaticity in the iron BCC to HCP phase transformation, J. of Chem. Phys 128 (2008) 104703.

[5] S. Mankovsky, S. Polesya, H. Ebert, W. Bensch, O. Mathon, S. Pascarelli, J. Minár, Pressure-induced BCC to HCP transition in Fe: Magnetism-driven structure transformation, Phys. Rev. B 88 (2013) 184108.

[6] Y. Chen, K. Ho, B. Harmon, First-principles study of the pressure-induced BCC-HCP transition in Ba, Phys. Rev. B 37 (1988) 283.

[7] R. M. Wentzcovitch, M. L. Cohen, Theoretical model for the HCP-BCC transition in Mg, Phys. Rev. B 37 (1988) 5571.

[8] P. Craievich, J. Sanchez, R. Watson, M. Weinert, Structural instabilities of excited phases, Phys. Rev. B 55 (1997) 787.

[9] J. Zhao, D. Maroudas, F. Milstein, Thermal activation of shear modulus instabilities in pressure-induced BCC–HCP transitions, Phys. Rev. B 62 (2000) 13799.

[10] G. Grimvall, B. Magyari-Köpe, V. Ozoliņš, K. A. Persson, Lattice instabilities in metallic elements, Rev. Mod. Phys. 84 (2012) 945.

[11] B. Feng, M. Widom, Elastic stability and lattice distortion of refractory high entropy alloys, Mat. Chem. Phys. 210 (2018) 309–314.

[12] S. Lee, R. Hoffmann, BCC and FCC transition metals and alloys: A central role for the Jahn-Teller effect in explaining their ideal and distorted structures, J. Am. Chem. Soc. 124 (2002) 4811–4823.

[13] K. Masuda-Jindo, S. Nishitani, V. Van Hung, HCP-BCC structural phase transformation of titanium: Analytic model calculations, Phys. Rev. B 70 (2004) 184122.

[14] H. A. Jahn, E. Teller, Stability of polyatomic molecules in degenerate electronic states - I-Orbital degeneracy, Proc. Roy. Soc. London A 161 (1937) 220–235.

[15] R. E. Peierls, Quantum Theory of Solids, Oxford, London, 1955.

[16] R. Englman, The Jahn-Teller effect in molecules and crystals, John Wiley & Sons, 1972.

[17] J. K. Burdett, S. Lee, Peierls distortions in two and three dimensions and the structures of AB solids, J. Am. Chem. Soc. 105 (1983) 1079–1083.

[18] G. Kresse, D. Joubert, From ultrasoft pseudopotentials to the projector augmented-wave method, Phys. Rev. B 59 (1999) 1758.

[19] J. P. Perdew, K. Burke, M. Ernzerhof, Generalized gradient approximation made simple, Phys. Rev. Lett. 77 (1996) 3865.

[20] M. de Jong, W. Chen, T. Angsten, A. Jain, R. Notestine, A. Gamst, M. Sluiter, C. K. Ande, S. van der Zwaag, J. J. Plata, C. Toher, S. Curtarolo, G. Ceder, K. A. Persson, M. Asta, Charting the complete elastic properties of inorganic crystalline compounds, Sci. Data 2 (2015) 150009.

[21] P. Souvatzis, O. Eriksson, M. Katsnelson, S. Rudin, Entropy driven stabilization of energetically unstable crystal structures explained from first principles theory, Phys. Rev. Lett. 100 (2008) 095901.

[22] A. Landa, J. Klepeis, P. Soderlind, I. Naumov, O. Velikokhatnyi, L. Vitos, A. Ruban, Ab initio calculations of elastic constants of the bcc vnb system at high pressures, J. Phys. Chem. Solids 67 (2006) 2056 – 2064, sMEC 2005.

[23] L. Koči, Y. Ma, A. Oganov, P. Souvatzis, R. Ahuja, Elasticity of the superconducting metals V, Nb, Ta, Mo, and W at high pressure, Phys. Rev. B 77 (2008) 214101.

[24] Y. X. Wang, H. Y. Geng, Q. Wu, X. R. Chen, Y. Sun, First-principles investigation of elastic anomalies in niobium at high pressure and temperature, J. Appl. Phys. 122 (2017) 235903.

[25] S. Baroni, S. De Gironcoli, A. Dal Corso, P. Giannozzi, Phonons and related crystal properties from density-functional perturbation theory, Rev. Mod. Phys. 73 (2001) 515.

[26] K. Persson, M. Ekman, V. Ozoliņš, Phonon instabilities in bcc Sc, Ti, La, and Hf, Phys. Rev. B 61 (2000) 11221–11224.

[27] W. Hume-Rothery, Researches on the nature, properties, and conditions of formation of intermetallic compounds, with special reference to certain compounds of tin, Ph.D. thesis, University of London (1926).

[28] H. Jones, The theory of alloys in the γ-phase, Proc. R. Soc. Lond. A 144 (1934) 225–234.

[29] H. Jones, N. Chako, The theory of brillouin zones and electronic states in crystals, Physics Today 15 (1962) 66.

[30] T. Fujiwara, T. Yokokawa, Universal pseudogap at fermi energy in quasicrystals, Phys. Rev. Lett. 66 (1991) 333–336.

[31] G. T. de Laissardière, D. Nguyen-Manh, D. Mayou, Electronic structure of complex Hume-Rothery phases and quasicrystals in transition metal aluminides, Prog. Mat. Sci. 50 (2005) 679–788.

[32] U. Mizutani, Hume-Rothery Rules for Structurally Complex Alloy Phases, CRC Press, Boca Raton, 2010.

[33] W. Setyawan, S. Curtarolo, High-throughput electronic band structure calculations: Challenges and tools, Comp. Mat. Sci. 49 (2010) 299–312.

[34] D. M. Ceperley, B. J. Alder, Ground state of the electron gas by a stochastic method, Phys. Rev. Lett. 45 (1980) 566–569.

[35] R. Feenstra, M. Widom, Wavetrans, http://www.andrew.cmu.edu/user/feenstra/wavetrans/.

[36] C. Kittel, Introduction to Solid State Physics, 8th Edition, Wiley, 2005.

[37] O. Hellman, P. Steneteg, I. A. Abrikosov, S. I. Simak, Temperature dependent effective potential method for accurate free energy calculations of solids, Phys. Rev. B 87 (2013) 104111.

[38] A. van de Walle, Q. Hong, S. Kadkhodaei, R. Sun, The free energy of mechanically unstable phases, Nat. Comm. 6 (2015) 7559.